The Pennsylvania State University
The Graduate School
College of Engineering

INITIAL RESIDUAL FORMULATION OF CTF

A Thesis in
Nuclear Engineering
by
Christopher A. Dances

© 2015 Christopher A. Dances

Submitted in Partial Fulfillment
of the Requirements
for the Degree of

Master of Science

May 2015

The thesis of Christopher A. Dances was reviewed and approved* by the following:

Maria Avramova
Associate Professor of Nuclear Engineering
Thesis Advisor, Chair of Committee

Kostadin Ivanov
Distinghuished Professor of Nuclear Engineering

Arthur Motta
Professor of Nuclear Engineering and Materias Science and Engineering
Chair of Nuclear Engineering

Vince Mousseau
Mentor from Sandia National Labs
Special Signatory

*Signatures are on file in the Graduate School.

Abstract

Nuclear engineering codes are being used to simulate more challenging problems and at higher fidelities than they were initially developed for. In order to expand the capabilities of these codes, state of the art numerical methods and computer science need to be implemented. One of the key players in this effort is the Consortium for Advanced Simulation of Light Water Reactors (CASL) and through development of the Virtual Environment for Reactor Applications (VERA). The sub-channel thermal hydraulic code used in VERA, COBRA-TF (Coolant-Boiling in Rod Arrays - Three Fluids), is partially developed at the Pennsylvania State University by the Reactor Dynamics and Fuel Management Research Group (RDFMG).

Currently, COBRA-TF solves 8 conservation equations for liquid, entrained droplet, and vapor phases of water boiling within the rod structure of a LWR reactor core. The conservation equations analytically reduce into a pressure matrix and are solved using a semi-implicit method. The solid conduction equations are then implicitly solved to determine the temperature within the fuel. Since the liquid solution is solved independent of the solid solution, the solid and liquid equations are explicitly coupled.

In an effort to help meet the objectives of CASL, a version of COBRTA-TF has been developed that solves the residual formulation of the 1D single-phase conservation equations. The formulation of the base equations as residuals allows the code to be run semi-implicitly or fully implicitly while clearly defining the original conservation equations. This paper outlines work to integrate 1D solid conduction equations into the residual formulation. This expands the solid liquid coupling to be either explicit or implicit. Different physical models, such as the homogeneous liquid solid energy model, can be readily implemented by adding the residual functions and variables. A simple test problem consisting of a single liquid channel and fuel pin was designed to compare the original version of COBRA-TF to the different numerical and physical models available through the new residual formulation. The methods are compared both for steady state and transient conditions to quantify the accuracy and stability of each method. The input parameters are varied over a variety of conditions to demonstrate when different methods are most appropriate. The ability to choose appropriate numerical methods and physical models will allow for greater fidelity, decrease computational expenses.

Table of Contents

List of Figures **vi**

List of Tables **viii**

List of Symbols **ix**

Acknowledgments **x**

Chapter 1
Introduction **2**

Chapter 2
Conservation Equations **3**
2.1 Single Phase Liquid Euler Equations 3
2.2 1-D Radial Solid Conduction Equation 5

Chapter 3
Residual Formulation **9**

Chapter 4
Isokinetic Step Advection **12**
4.1 Problem Setup 12
4.2 Density Advection and Error 13
4.3 Modified Equation Analysis 14
4.4 Scaling of Error 15

Chapter 5
Shock Tube **18**
5.1 Problem Setup 18
5.2 Analytical Solution 19
5.3 Results and Error 20
5.4 Scaling of Error 23

Chapter 6
Isokinetic Sine Wave Advection **24**
6.1 Problem Setup 24
6.2 Code Convergence 26

6.3 Modified Equation Analysis 26
6.4 Richardson Extrapolation 28
6.5 Convergence of Error 28
6.6 Order of Accuracy 30

Chapter 7
Uniform Heating Problem **32**
7.1 Problem Setup 32
7.2 Steady State Analytical Solution 33
7.3 Steady State Results 33
7.4 Transient Results 35

Bibliography **36**

List of Figures

2.1 The finite volume structure for COBRA-TF 3
2.2 Radial Rod Meshing 6
2.3 Radial Rod Meshing 7

3.1 Strucutre of the jacobian matrix for single phase liquid 10
3.2 Strucutre of jacobian matrix for single phase liquid explicitly coupled to solid conduction 11
3.3 Strucutre of the jacobian matrix for single phase liquid implicitly coupled to solid conduction 11

4.1 Setup for the isokinetic advection problem 12
4.2 Comparison of density advection to analytical solution 13
4.3 Scaling of numerical error with constant time step size for density 16
4.4 Temporal Order of Accuracy for density 16
4.5 Advection of isokinetic density wave $\frac{kg}{m^3}$ in time and space for CFL=1 17

5.1 Setup for the shock tube problem 18
5.2 Regions within the shock tube based on rarefaction and compression 20
5.3 Comparison of analytical and numerical results for shock tube 21
5.4 Truncation error for shock tube 22
5.5 Richardson Extrapolation of the shock tube results N=50 23
5.6 Temporal Order of Accuracy for shock tube 23

6.1 Enthalpy Near the Inlet and the Analytical Solution 25
6.2 Density Near the Inlet and the Analytical Solution 26
6.3 Code Convergence Criteria for the Original Version of CTF 27
6.4 Summation of the Residuals for the Residual Version of CTF 27
6.5 Difference Between Successive Temporal Refinements for Density 29
6.6 Difference Between Successive Spatial Refinements for Density 29
6.7 Temporal Order of Accuracy 30
6.8 Spatial Order of Accuracy 31

7.1 Steady State Radial Temperature Distribution Difference to Rod Surface Temperature 34
7.2 Error of Different Numerical Methods to Analytical Solution 34
7.3 Steady State Axial and Radial Temperature Distribution in the Fuel Rod 35

7.4 Plot of the Radial Nodal Temperatures for the Semi-Implicit Method 36
7.5 Plot of the Radial Nodal Temperatures for the Implicit Method 36
7.6 Temperature profile over time for the Semi-Implicit Method 37
7.7 Temperature profile over time for the Implicit Method 37

List of Tables

4.1 Input Parameters for Isokinetic Advection 13

5.1 Input Parameters for Shock Tube Verification Probelm 19

6.1 Problem Parameters 25

7.1 Problem Parameters 32
7.2 Relative Error of Difference Between Fuel Centerline to Rod Surface Temperature 34

List of Symbols

ρ	Density
h	Enthalpy
u	Velocity
P	Pressure
t	Time
g	Gravitional Acceleration

Acknowledgments

The Constortium for the Advanced Simulation of Light Water Reactors (CASL) The Reactor Dynamics Fuel Management Group (RDFMG) at Penn State The Toshiba Westinghouse Fellows Program

Dedication

To my parents, and everyone who has supported me in this.

Chapter 1 Introduction

For the past several decades, the primary focus in nuclear engineering within the United States has been on light water reactors (LWR). Commercially, all nuclear reactors are either boiling water reactors (BWR) or pressurized water reactors (PWR). Correct computation of the thermal hydraulics within the reactor core leads to efficient design and accuracy in the safety analysis. A popular subchannel code for modeling the hydrodynamics within the reactor core is CTF, which is a subchannel thermal-hydraulics code developed from COBRA-TF [1]. This FORTRAN based code solves 8 conservation equations for liquid, entrained droplet, and vapor phases phases, plus one conservation equation for non-condensable gases. A 1-D residual formulation of the code has been created. While other residual formulations have been formed for other versions of COBRA-TF [2], none have been integrated into the CASL version of CTF. The current version of CTF has standard verification practices that focus on software quality engineering similar to those in other versions of COBRA-TF [3], but lacks an in depth verification document that focuses on numerical algorithm verification. This paper focues on this second type of verification and outlines the initial verification of the original version of the code as well as the residual version of the code. The verification problem is a single phase 1-D channel with transient inlet density and mass flow rate. The problem will undergo a Richardson's extrapolation in the temporal and spatial domains to verify the convergence and order of accuracy of the error. The study of the order of accuracy is considered one of the more rigorous verification criteria [4]. This work will be expanded to perform verificaiton on the single phase equations in both axial and transverse dimensions [5], and coupled multiphysics [6].

Chapter 2
Conservation Equations

2.1 Single Phase Liquid Euler Equations

The finite volume structure in COBRA-TF in figure 2.1 is for a one-dimmensional channel in the axial direction with n number of cells. The first and last cells at 0 and $n+1$ are ghost cells and act as the boundary conditions for the problem. Pressure, enthalpy, and density are averaged over the cell volume and are located at the center of the cell. Mass flow rate and velocity are located at the faces in between cells. The cells are represented with an index i, and the faces with indexes of $i+\frac{1}{2}$ or $i-\frac{1}{2}$. This project will initially focus on this 1-D configuration. Usually the code is three dimensional, with channels connecting to each other in two more dimmensions. Fully 3-D equations will be considered in future work.

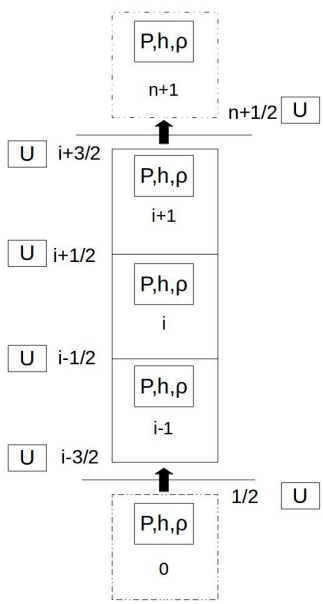

Figure 2.1. The finite volume structure for COBRA-TF

The thermal hydraulics of a LWR core is an important part of nuclear reactor desigin. COBRA-TF solves 8 conservation equations for liquid, entrained droplet, and vapor phases of water boiling within the rod structure of a LWR reactor core [1]. Currently, the conservation equations analytically reduce into a pressure matrix in a semi-implicit method with rod temperatures solved for explicitly. This work involves representing the 1-D single phase liquid conservation equations and calculated variables in a residual formulation. The full jacobian matrix can then be built numerically, and can then either be reduced to a pressure matrix or solved directly. Verification of the residuals was done by comparing calculated results to analytical solutions for isokinetic advection and shock tube problems. For each verification problem, a scaling study of the truncation error was compared to the predicted behaviour derived from modified equation analysis using Richardson extrapolation. Further work was then applied to represent 1-D heat conduction within the heater rods. Some initial work was done to allow the code to solve either semi-implicitly, or fully impicitly. The single phase Euler partial differential equations for mass (2.1), momentum (2.2), and energy (2.3) corresond to the unknown variables density ρ, velocity u, pressure P, and enthalpy h. The first terms in each of the equations are temporal terms. The rest of the terms are steady state spatial terms. The last term in the energy equation represents the net heat transfer from the adjacent rods to the current fluid subchannel.

$$\frac{\partial \rho}{\partial t} + \bigtriangledown \rho u = 0 \tag{2.1}$$

$$\frac{\partial \rho u}{\partial t} + \bigtriangledown \rho u^2 + \bigtriangledown P - \rho g = 0 \tag{2.2}$$

$$\frac{\partial \rho h}{\partial t} - \frac{\partial P}{\partial t} + \bigtriangledown (\rho u h) + \frac{q_{rod}}{\forall_{fluid}} = 0 \tag{2.3}$$

The 1-D formulation of the Euler Equations will assume a direction x as shown in the 1-D mass equation (2.4). The momentum and energy equations are represented in a non-conservative form as shown in equations (2.5) and (2.7). The momentum equation contains a term that has a product of the left hand side of the 1-D mass equation. This terms can therefore be dropped since it is equivalent to zero, and the entire equation can be divided by density to give a simpler form of the momentum equation (2.6). The last term in the energy equation represents the net heat transfer from the adjacent rods to the current fluid subchannel. This is equated as the surface area of the rod liquid interface times the heat transfer coefficient and temperature difference between the wall and bulk fluid temperatures.

$$\frac{\partial \rho}{\partial t} + \frac{\partial \rho u}{\partial x} = 0 \tag{2.4}$$

$$\rho \frac{\partial u}{\partial t} + u \left(\frac{\partial \rho}{\partial t} + \frac{\partial \rho u}{\partial x} \right) + \rho u \frac{\partial u}{\partial x} + \frac{\partial P}{\partial x} - \rho g = 0 \tag{2.5}$$

$$\frac{\partial u}{\partial t} + u \frac{\partial u}{\partial x} + \frac{1}{\rho} \frac{\partial P}{\partial x} - g = 0 \tag{2.6}$$

$$\rho\frac{\partial h}{\partial t} - \frac{\partial P}{\partial t} + h\frac{\partial \rho}{\partial t} + \rho u\frac{\partial h}{\partial x} + h\frac{\partial \rho u}{\partial x} + \frac{2\pi r_{rod}}{A_i}h_l\left(T_{wall} - T_{fluid}\right) = 0 \tag{2.7}$$

The 1-D equations are then evaluated at a position index i and a certian time n in order to solve for the next time value of $n+1$. In the mass equation (2.8), the velocities are located at the cell faces $i+\frac{1}{2}$ and $i-\frac{1}{2}$. The density at a corresponding face is either upwinded $\dot{\rho}^n_{i+\frac{1}{2}}$, or averaged $\bar{\rho}^n_{i+\frac{1}{2}}$. In equation (2.9), the derivative $\frac{\partial u}{\partial x}$ is upwinded assuming that the flow is positive. In the energy equation, (2.10) the enthalpy values in the first spatial term are upwinded and shown here assuming a positive velocity. The equation of state (2.11) solves for density assuming that it is a linear combination of changes due to pressure and enthalpy. The partial derivatives in the equation are calculated from steam tables as functions of old time pressure and enthalpy.

$$\frac{\rho_i^{n+1} - \rho_i^n}{\Delta t} + \frac{\dot{\rho}^n_{i+\frac{1}{2}}u^{n+1}_{i+\frac{1}{2}} - \dot{\rho}^n_{i-\frac{1}{2}}u^{n+1}_{i-\frac{1}{2}}}{\Delta x} = 0 \tag{2.8}$$

$$\frac{u^{n+1}_{i+\frac{1}{2}} - u^n_{i+\frac{1}{2}}}{\Delta t} + u^n_{i+\frac{1}{2}}\left(\frac{u^n_{i+\frac{1}{2}} - u^n_{i-\frac{1}{2}}}{\Delta x}\right) + \frac{1}{\bar{\rho}^n_{i+\frac{1}{2}}}\frac{P^{n+1}_{i+1} - P^{n+1}_i}{\Delta x} - g = 0 \tag{2.9}$$

$$\begin{aligned}\rho_i^n\frac{h_i^{n+1} - h_i^n}{\Delta t} + h_i^n\frac{\rho_i^{n+1} - \rho_i^n}{\Delta t} - \frac{P_i^{n+1} - P_i^n}{\Delta t} + (\rho u)_i^n\frac{h_i^n - h_{i-1}^n}{\Delta x} \\ + h_i^n\frac{\dot{\rho}^n_{i+\frac{1}{2}}u^{n+1}_{i+\frac{1}{2}} - \dot{\rho}^n_{i-\frac{1}{2}}u^{n+1}_{i-\frac{1}{2}}}{\Delta x} + \frac{2\pi r_{rod}}{A_i}h_l\left(T_{wall} - T_{fluid}\right) = 0\end{aligned} \tag{2.10}$$

$$\rho_i^{n+1} - \rho_i^n = \left(\frac{\partial \rho}{\partial P}\right)\left(P_i^{n+1} - P_i^n\right) + \left(\frac{\partial \rho}{\partial h}\right)\left(h_i^{n+1} - h_i^n\right) \tag{2.11}$$

2.2 1-D Radial Solid Conduction Equation

The conduction equation for a cylindrical system is given in equation 2.12. The first term represents the amount of energy stored within the solid area within a unit time. The second term is the conduction in the radial direction. The second and third terms are the conduction in the azimuthal and axial directions, respectively. The last term represents the heat generation within the solid.

$$\rho_i c_{p,i}\frac{\partial T}{\partial t} - \frac{1}{r}\frac{\partial}{\partial r}\left(kr\frac{\partial T}{\partial r}\right) - \frac{1}{r^2}\frac{\partial}{\partial \theta}\left(k\frac{\partial T}{\partial \theta}\right) - \frac{\partial}{\partial z}\left(k\frac{\partial T}{\partial z}\right) - q''' = 0 \tag{2.12}$$

This work focuses on the 1D radial equations setting the derivatives with respect to the angular and axial directions to zero. Equation 2.12 now reduces to equation 2.13.

$$\rho_i c_{p,i}\frac{\partial T}{\partial t} - \frac{1}{r}\frac{\partial}{\partial r}\left(kr\frac{\partial T}{\partial r}\right) - q''' = 0 \tag{2.13}$$

When the radius is zero, the fuel temperature is considered to be a maximum giving the

boundary condition in equation 2.14

$$\left(\frac{\partial T}{\partial r}\right)_{r=0} = 0 \tag{2.14}$$

The nuclear rod geometry types in CTF are meshed at each axial level according to figure 2.2 where the red region is fuel and the grey region is cladding. The black dots represent the nodes within the fuel. Each node covers a region within the rod as bounded by the dashed lines. The nodes within the fuel are located at the center of the region. Each region is assumed to have uniform properties with values evaluated at the node. The last node within the fuel is located at the surface of the fuel at the interface with the gap. There are two additional nodes that represent the outer clad surface and the inner clad surface respectively. The gap between the outer surface of the fuel and the inner surface of the cladding has a specified heat transfer coefficient or is calculated using the dynamic gap conductance model.

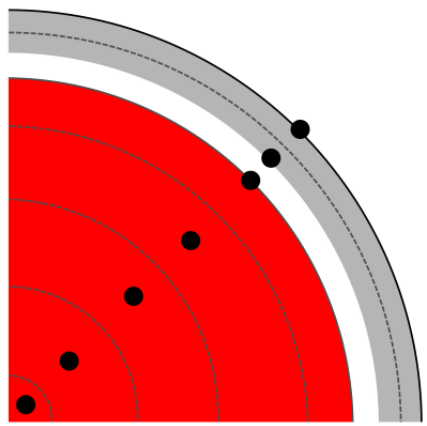

Figure 2.2. Radial Rod Meshing

The outer surface of the cladding is assumed to be in contact with the fluid in the adjacent channel on that axial level. The rods have the same number of axial levels as the fluid, but do not have ghost cells at the top and bottom. Instead the first and last fluid axial levels are connected to two rod axial levels as shown by Figure 2.3, where the rod axial levels are on the left, and the fluid axial levels are on the right. The light blue cells are the fluid ghost cells.

The conduction equation can be approximated using the finite difference method, or the control volume difference method [7]. The control volume method will be used since it is the same method utilized in the original version of CTF. The implicit finite difference equation now looks like equation 2.15.

$$\rho_i c_{p,i} \frac{T_i^{n+1} - T_i^n}{\Delta t} - \frac{2\pi}{A_i}\left(\left(k_{i+\frac{1}{2}} r_{i+\frac{1}{2}} \frac{T_{i+1}^{n+1} - T_i^{n+1}}{\Delta r_{i+\frac{1}{2}}}\right) - \left(k_{i-\frac{1}{2}} r_{i-\frac{1}{2}} \frac{T_i^{n+1} - T_{i-1}^{n+1}}{\Delta r_{i-\frac{1}{2}}}\right)\right) - q_i''' = 0 \tag{2.15}$$

The density on the temporal term is defined as the cold mass of the node divided by the current volume of the node, so that mass is not lost in the presence of expansion. The temporal

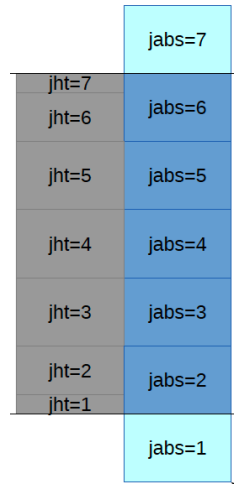

Figure 2.3. Radial Rod Meshing

derivative is approximated with first order accurate forward differencing. The spatial derivatives are evaluated at the right boundary, $i+\frac{1}{2}$, and at the left boundary,$i-\frac{1}{2}$ using first order forward differencing. When $i=1$ at the inner most node, the radius at the left boundary and the derivative of the temperature is zero. At the boundary between the surface of the fuel and the inside surface of the cladding, a different set of finite difference equations are needed as given by equation 2.16

$$\rho_i c_{p,i}\frac{T_i^{n+1}-T_i^n}{\Delta t}+\frac{2\pi}{A_i}\left(k_{i-\frac{1}{2}}r_{i-\frac{1}{2}}\frac{T_i^{n+1}-T_{i-1}^{n+1}}{\Delta r_{i-\frac{1}{2}}}\right)-\frac{2\pi r_i h_{gap}}{A_i}\left(T_{i+1}^{n+1}-T_i^{n+1}\right)-q_i'''=0 \quad (2.16)$$

The finite difference equation between the inner and outer cladding surfaces given by equation 2.17 has no heat generation or conduction from the fuel. Instead the volumetric heat rate is calculated using the term for the volumetric heat rate across the gap and a similar term but for the volumetric heat rate across the cladding. Since the cladding does not have any heat generation, this term is represented as the temperature difference across the cladding times the thermal resistance across the cladding times the perimeter of the cladding divided by the area of the inner cladding region.

$$\rho_i c_{p,i}\frac{T_i^{n+1}-T_i^n}{\Delta t}+\frac{2\pi r_i h_{gap}}{A_i}\left(T_i^{n+1}-T_{i-1}^{n+1}\right)-\frac{2\pi}{A_i}\left(k_{i+\frac{1}{2}}r_{i+\frac{1}{2}}\frac{T_{i+1}^{n+1}-T_i^{n+1}}{\Delta r_{i+\frac{1}{2}}}\right)=0 \quad (2.17)$$

The finite difference equation between the inner and outer cladding surfaces given by equation 2.18 relates the wall temperature to the bulk fluid temperature at the same axial level. The volumetric heat rate lost to the fluid is represented as the temperature difference between the wall and the fluid times the thermal resistance of the fluid and divided by the outer cladding region.

$$\rho_i c_{p,i} \frac{T_i^{n+1} - T_i^n}{\Delta t} + \frac{2\pi}{A_i} \left(k_{i-\frac{1}{2}} r_{i-\frac{1}{2}} \frac{T_i^{n+1} - T_{i-1}^{n+1}}{\Delta r_{i-\frac{1}{2}}} \right) - \frac{2\pi r_i h_{fluid}}{A_i} \left(T_i^{n+1} - T_{fluid}^k \right) = 0 \tag{2.18}$$

The numerator in the last term is also in the fluid energy conservation equation. The heat transfer coefficient is currently calculated using the Dittus-Boelter correlation. The fluid properties are evaluated at the bulk fluid temperature. When the fluid finite equations are solved for implicitly, they will impact the solid conduction equations through the calculation of the heat transfer coefficient and the fluid temperature.

Chapter 3
Residual Formulation

A residual is simply the difference between the value at some future time $n+1$ and the value at the current iteration k. This can be applied to desired variables as shown in equations (3.1), (3.2), (3.3), and (3.4). Residuals can also be applied to the conservation equations by substituting the definition of the residual variables into the conservation equations. This will effectively change any variables evaluated at $n+1$ to k. Each cell will have three residual variables and three residual equations. For the entire solution, we will then have a residual variable array δX, and a residual function array $F(X)$ which defines a linear system as seen in equation (3.5).

$$\delta P_i = P_i^{n+1} - P_i^k \tag{3.1}$$

$$\delta h_i = h_i^{n+1} - h_i^k \tag{3.2}$$

$$\delta u_{i+\frac{1}{2}} = u_{i+\frac{1}{2}}^{n+1} - u_{i+\frac{1}{2}}^k \tag{3.3}$$

$$\delta \rho_i = \rho_i^{n+1} - \rho_i^k \tag{3.4}$$

$$J\delta X = -F(X) \tag{3.5}$$

The Jacobian matrix is defined in equation (3.6) as the derivative of each response of the function F_j with respect to each variable X_i. The derivative can be calculated numerically as shown by equation (3.7) where ϵ is a small numerical value. For COBRA-TF the equations are linear, and this numerical approximation of the Jacobian matrix is exact. This should produce the same jacobian matrix that COBRA-TF currently generates analytically.

$$J_{i,j} = \frac{\partial F_j(X)}{\partial X_i} \tag{3.6}$$

$$J_{i,j} \approx \frac{F_j(X_i + \epsilon) - F_j(X)}{\epsilon} \tag{3.7}$$

To build the jacobian matrix, an object oriented class was created that contains three arrays. An array that points to the residual functions, an array that points to the position within a target variable arrray, and an array that has the index that the function is to be evaluated at. These lists can be appended to in any order, but have to be appended all at the same time so that variables and functions must correspond with each other. Then to construct the jacobian matrix, the residual function and residual variable arrays can each be looped over to numerically build the jacobian matrix as seen in figure 3.1.

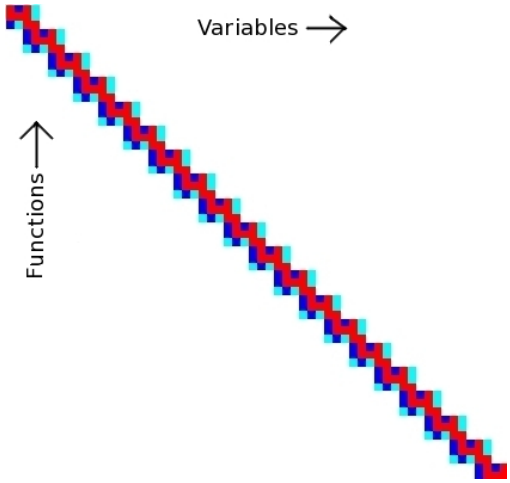

Figure 3.1. Strucutre of the jacobian matrix for single phase liquid

The explicitly coupled solid liquid Jacobian matrix can be seen in figure 3.2, where blue values represent negative entries and red values positive entries. The black lines were drawn on top of the image to represent artificial boundaries between the liquid Jacobian matrix in the top left corner and the solid Jacobian matrix in the top right corner.

The fluid Jacobian matrix contains 3 conservation equations for every axial level. The liquid function residuals are appended in the order of mass conservation, energy conservation, and momentum conservation for each axial level. These correspond the pressure, enthalpy, and velocity at each axial level. The liquid Jacobian matrix can be evaluated as either semi-implicit or fully implicit. The solid Jacobian matrix contains 1 energy conservation equation for each node in the rod. Since axial and azimuthal conduction are not computed, each radial level is computed separately from the rest. This can be seen by the lack of cross terms in the Jacobian matrix at each axial level. The Jacobian matrix on the right is an implicit coupling between the implicit liquid Jacobian matrix and the implicit solid matrix. The cross terms in the top right corner represent the effect of the wall temperature on the energy equation in the liquid Jacobian matrix. The terms on the bottom left represent the effects of pressure, enthalpy, and velocity on the energy equation in the solid Jacobian matrix. The implicit matrix is unconditionally stable, allowing for time steps greater than the material Courant limits. Once the coupled Jacobian matrix is constructed, it is solved using the linear Krylov solver from PETSC. The residuals for each of the conservation equations are then L2 normalized over the domain to determine the convergence of the system.

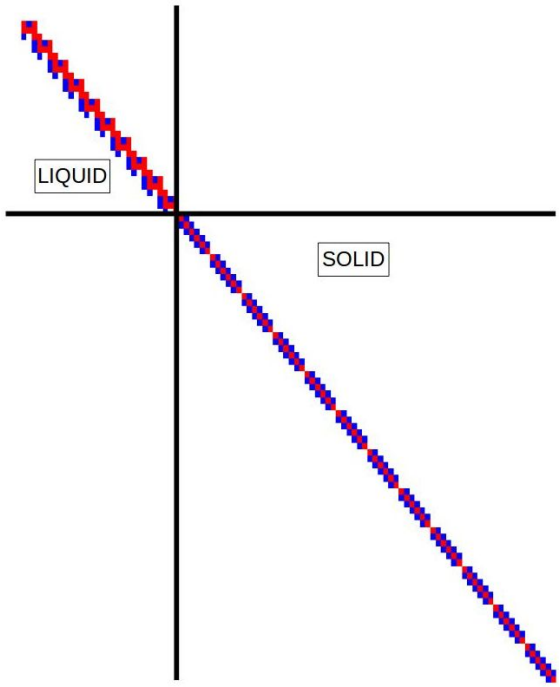

Figure 3.2. Strucutre of jacobian matrix for single phase liquid explicitly coupled to solid conduction

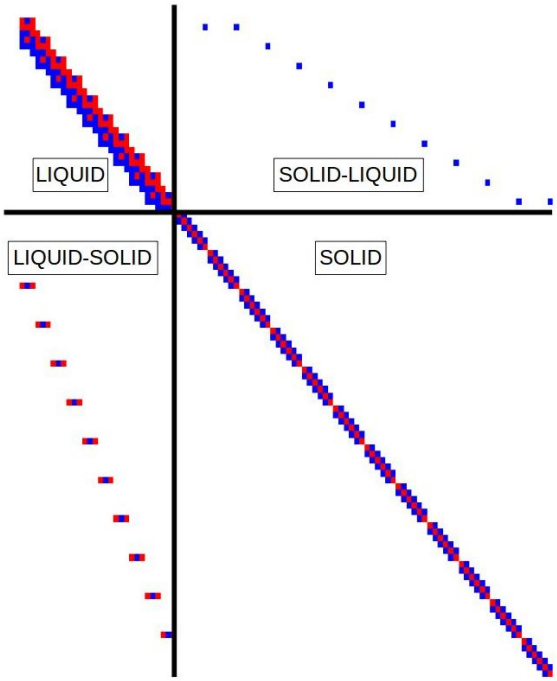

Figure 3.3. Strucutre of the jacobian matrix for single phase liquid implicitly coupled to solid conduction

Chapter 4
Isokinetic Step Advection

4.1 Problem Setup

A tube with no gravity acting in the direction of fluid flow has an initial condition of $U_1, \rho_1, h_1, P_1, \dot{m}_1$ everywhere except at the starting position that has an intitial conditions of $h_2, \rho_2, \dot{m}_2$. When the time step for the calcuation is taken be exactly equal to the CFL number as seen in equation 4.1, the inlet conditions should advect through the rest of the system in the form of a square wave. This is a unique situation where the CFL can be held constant throughout the simulation, and where the spatial and temporal trucation error can cancel each other out at $CFL = 1$. When the CFL is less than 1, numerical diffusion occurs based on the truncation terms produced by the modified equation analysis.

$$CFL = \frac{\Delta t U_0}{\Delta x} \tag{4.1}$$

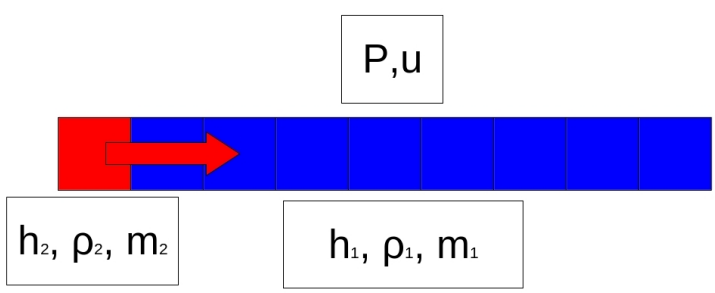

Figure 4.1. Setup for the isokinetic advection problem

The problem was set up using the parameters given in table 4.1. Initial temperature, density, and mass flow rate of the sysmte differs from the inlet temperature, density, and mass flow rate. The pressure and velocity of the system remains constant. The transient runs until the center of the advected wave reaches the end of the tube at roughly 60 seconds. The value of the parameters are more or less arbitrary, but approximate a single channel about the length of a fuel assembly undergoing a 10 C temperature difference. The water is close to standard temperature and

pressure.

Table 4.1. Input Parameters for Isokinetic Advection

Length	3.00	m
Channel Area	0.0001	m^2
Wetted Perimeter	0.040	m
Pressure	1.00	bar
Initial Temperature	40.00	C
Inlet Temperature	30.00	C
Inlet Mass Flow Rate	0.005	kg/s
Inlet Density	992.61	kg/m^3
Velocity	0.050372	m/s

4.2 Density Advection and Error

Figure 4.2 compares the analytical and numerical advection of density through the domain for a CFL number of 0.500. The higher density in the colder region is on the left, and the lower density of the warmer region is on the right. The red line on the right of the figure depicts the truncation error at the current time step. The truncation error occurs around the original dicontinuity as it advects through the solution. As the discontinuity propogates it becomes more diffuse spatially. Once it reaches the outlet the discontiuty leaves the domain and the overall error drops to nearly zero. For this problem, the truncation error can be shown to be a direct function of the CFL number and can be reduced to nearly zero throughout the simulation. This simplified problem with an exact solution is used for code verification.

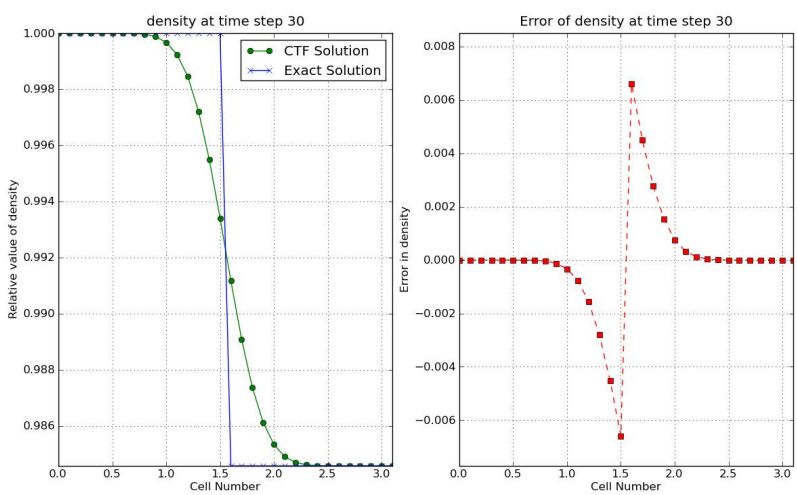

Figure 4.2. Comparison of density advection to analytical solution

4.3 Modified Equation Analysis

For this isokinetic problem, the original mass balance equation can be re-written to look like equation 6.3. Using upwinding, the finite difference can be written to look like equation 6.4. A second order Taylor series approximation can be used for ρ_i^{n+1} and ρ_{i-1}^n as shown in equations 6.5 and 6.6 respectively. The higher order terms ($O(\Delta x^2, \Delta t^2)$) are not taken into account for this approximation. The Taylor series approximations can then be substituted into 6.4 to yield 6.7. This is the beginning of the modified equation analysis. The goal will be to isolate the original PDE and define the truncation error.

$$\frac{\partial \rho}{\partial t} + U_0 \frac{\partial \rho}{\partial x} = 0 \tag{4.2}$$

$$\frac{\rho_i^{n+1} - \rho_i^n}{\Delta t} + U_0 \frac{\rho_i^n - \rho_{i-1}^n}{\Delta x} = 0 \tag{4.3}$$

$$\rho_i^{n+1} = \rho_i^n + \frac{\partial \rho}{\partial t}\Delta t + \frac{1}{2}\frac{\partial^2 \rho}{\partial t^2}\Delta t^2 + O(\Delta t^3) \tag{4.4}$$

$$\rho_{i-1}^n = \rho_i^n - \frac{\partial \rho}{\partial x}\Delta x + \frac{1}{2}\frac{\partial^2 \rho}{\partial x^2}\Delta x^2 + O(\Delta x^3) \tag{4.5}$$

The lengthy equation 6.7 can be reduced to equation 6.8 since the ρ_i^n terms subtract out and the Δt and Δx terms in the denominator cancel out. This reduced equation can the be re-written into equation 6.9, with the original PDE followed by the truncation terms. Notice how the terms on the right are dependent on both the numerical spacing Δt and Δx, but also on the second derivatives of density with respect to space and time.

$$\frac{\left(\rho_i^n + \frac{\partial \rho}{\partial t}\Delta t + \frac{1}{2}\frac{\partial^2 \rho}{\partial t^2}\Delta t^2\right) - \rho_i^n}{\Delta t} + U_0 \frac{\rho_i^n - \left(\rho_i^n - \frac{\partial \rho}{\partial x}\Delta x + \frac{1}{2}\frac{\partial^2 \rho}{\partial x^2}\Delta x^2\right)}{\Delta x} + O(\Delta x^2, \Delta t^2) = 0 \tag{4.6}$$

$$\frac{\partial \rho}{\partial t} + \frac{1}{2}\frac{\partial^2 \rho}{\partial t^2}\Delta t + U_0\left(\frac{\partial \rho}{\partial x} - \frac{1}{2}\frac{\partial^2 \rho}{\partial x^2}\Delta x\right) + O(\Delta x^2, \Delta t^2) = 0 \tag{4.7}$$

$$\frac{\partial \rho}{\partial t} + U_0 \frac{\partial \rho}{\partial x} + \frac{1}{2}\frac{\partial^2 \rho}{\partial t^2}\Delta t - U_0 \frac{1}{2}\frac{\partial^2 \rho}{\partial x^2}\Delta x + O(\Delta x^2, \Delta t^2) = 0 \tag{4.8}$$

Before we can procede, we need to take the derivative of the original PDE with respect to space and time as shown in equations 4.9 and 4.10 respectively. These two derivatives can substitute into each other using the common term $\frac{\partial^2 \rho}{\partial x \partial t}$. The second derivatives of density with respect to space and time are therefore related by the velocity squared as shown by equation 4.11.

$$\frac{\partial^2 \rho}{\partial t^2} + U_0 \frac{\partial^2 \rho}{\partial x \partial t} = 0 \tag{4.9}$$

$$\frac{\partial^2 \rho}{\partial t \partial x} + U_0 \frac{\partial^2 \rho}{\partial x^2} = 0 \tag{4.10}$$

$$\frac{\partial^2 \rho}{\partial t^2} = U_0^2 \frac{\partial^2 \rho}{\partial x^2} \tag{4.11}$$

This relationship can then be substituted back into equation 6.9, which can be reduced to equation 4.13 after igonoring the higher order terms. The error depends on the CFL number, the axial spacing, and the second order derivative of density with respect to space. This derivative is what gives the error the characterisitcs of diffusion. When the CFL number is less than one, the error term is negative and the diffusion is dampening. When the CFL number is greater than one, the error term becomes positive, and the accumulation of the error destabilizes the solution.

$$\frac{\partial \rho}{\partial t} + U_0 \frac{\partial \rho}{\partial x} - \frac{1}{2}\left(\Delta x U_0 \frac{\partial^2 \rho}{\partial x^2} - U_0^2 \frac{\partial^2 \rho}{\partial x^2} \Delta t\right) + O(\Delta x^2, \Delta t^2) = 0 \tag{4.12}$$

$$\frac{\partial \rho}{\partial t} + U_0 \frac{\partial \rho}{\partial x} - \frac{\Delta x U_0}{2} \frac{\partial^2 \rho}{\partial x^2} (1 - CFL) + O(\Delta x^2, \Delta t^2) = 0 \tag{4.13}$$

Modified eqauation analysis can be applied to the energy balance equation presented in equation 4.14. The energy equation is presented in a form where the momentum equation was substituted in as zero and then divided through by density. The result presented in equation 4.15 is similar in form to the result for the mass balance equation 4.13.

$$\frac{\partial h}{\partial t} - \frac{1}{\rho} \frac{\partial P}{\partial t} + U_0 \frac{\partial h}{\partial x} = 0 \tag{4.14}$$

$$\frac{\partial h}{\partial t} - \frac{1}{\rho} \frac{\partial P}{\partial t} + U_0 \frac{\partial h}{\partial x} - \frac{\Delta x U_0}{2} \frac{\partial^2 h}{\partial x^2} (1 - CFL) = 0 \tag{4.15}$$

4.4 Scaling of Error

From the modifed equation analysis, the advection problem should prove to be first order accurate in time and space. Assuming a fixed number of points, the time step was halved several times. The relative difference between each step was taken and $\ell 1$ normalized across space at at a particular time. The plot of this difference can be seen for density in figure 4.3.

The power fit for density has a high correlation coefficient, and shows that the order of accuracy temporally is close to 1. Richardson extrapolation to determine the order of accuracy at each point as shown by figure 4.4. As the time step size decreases, the order of accuracy approaches 1.0 due to smaller higher order terms.

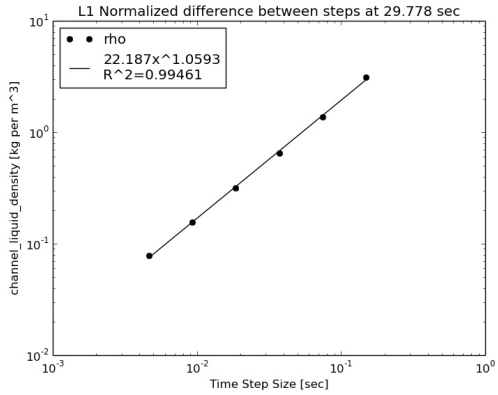

Figure 4.3. Scaling of numerical error with constant time step size for density

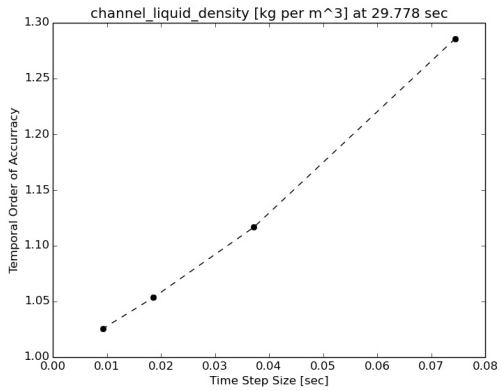

Figure 4.4. Temporal Order of Accuracy for density

When the CFL number is set to 1, the spatial error and temporal error cancel out producing a perfect square wave in time and space as shown by figure 4.5. This holds true for a variety of spatial mesh sizes, confirming that both the temporal and spatial errors are first order accurate.

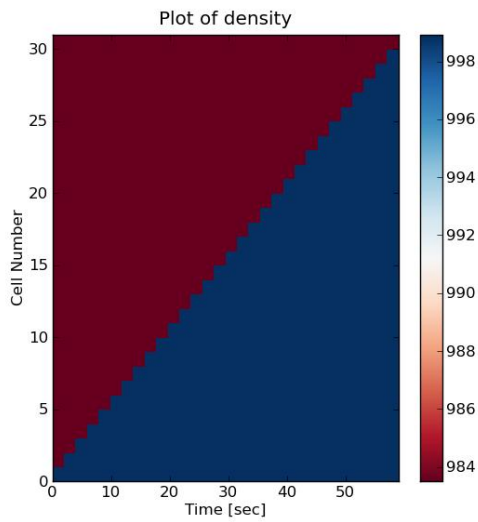

Figure 4.5. Advection of isokinetic density wave $\frac{kg}{m^3}$ in time and space for CFL=1

Chapter 5
Shock Tube

5.1 Problem Setup

A shock tube is a very common and standard method of verification for momentum and pressure. However, an exact analytical solution is more readily obtained for an ideal gas such as air. A shock tube is created by setting the initial mass flow rate and velocity to zero with no gravity. The boundary conditions at the inlet and outlet are also set to zero, simulating a closed system. A region of high pressure is defined for one half of the domain, and a region of low pressure for the second half. An imaginary diaphragm divides the two regions before the simulation, and at $t = 0$ disappears.

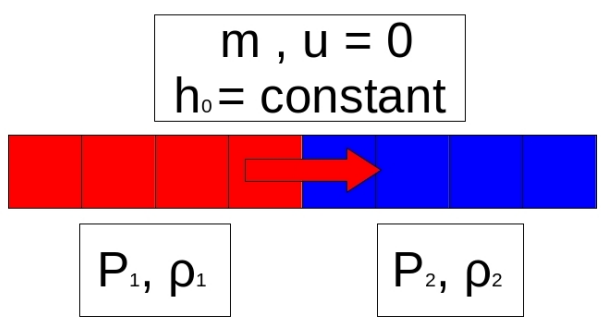

Figure 5.1. Setup for the shock tube problem

The problem was set up using the parameters given in table 5.1. The geometry is similar to the previous problem, but the length of the tube was elongated to take into account the faster propogation of the rarefaction and compression waves. The temperature and pressure of the air are near standard conditions.

Each region has a unique density corresponding to the different pressures using the equation of state for air given in equation 5.1 where $\gamma = 1.4$ is the ratio of specific heats for air. Additionally, the specific heat $Cp = 1.005\frac{kJ}{kg-K}$ to convert between enthalpy and temperature. The initial enthalpy of the system is constant, but will change non-uniformly as a function of time. The

Table 5.1. Input Parameters for Shock Tube Verification Probelm

Length	25.00	m
Channel Area	0.0001	m^2
Wetted Perimeter	0.040	m
Initial Pressure	1.00	bar
Initial Enthalpy	304.66575	kJ/kg
Initial Mass Flow Rate	0.000	kg/s
Initial Pressure Drop	0.09576	bar

velocity is initially set to zero, but will change as the compression and rarefaction waves move. Since the velocity is set to zero initially, it can't be used to evaluate the time step size. Instead the speed of sound can be evaluated using equation 5.2, and this velocity can be used to calculate the time step. While there might be some slight change in the speed of sound due to enthalpy changes, it should remain effectively constant.

$$\rho = \left(\frac{\gamma}{\gamma - 1}\right)\frac{P_{abs}}{h} \tag{5.1}$$

$$a = \sqrt{(\gamma - 1)\, h} \tag{5.2}$$

$$\gamma = \frac{C_p}{C_v} \tag{5.3}$$

5.2 Analytical Solution

When the diaphragm disappears, a compression wave will move to the right and a rarefaction wave to the left. These two waves split the domain into four distinct regions. There is a region to the left of the rarefaction wave that has the same properties as the initial left region. There is a region between the rarefaction wave and the initial location of the diaphragm. There is a region between the initial location of the diaphragm and the compression wave. There is a region to the right of the compression wave, that has the same properties as the initial right region. The analytical solution does not take into account reflection off of the walls, however the numerical solution can due to the applied boundary conditions for mass flow rate.

For a perfectly caloric gas, the following equations are provided [8, p. 238] given the initial conditions for state 1 and 4 in conjuction with equation 5.2. An iterative method is required to solve 5.4 for $\frac{P_2}{P_1}$. Once the region properties are obtained, the regions themselves are mapped by comparing the current position and time to the velocity of the rarefaction and compression wave.

$$\frac{P_4}{P_1} = \frac{P_2}{P_1}\frac{\left(1 - (\gamma - 1)(\frac{a_1}{a_4})(\frac{P_2}{P_1} - 1)\right)^{-\frac{2\gamma}{\gamma - 1}}}{\sqrt{2\gamma\left[2\gamma + (\gamma + 1)(\frac{P_2}{P_1} - 1)\right]}} \tag{5.4}$$

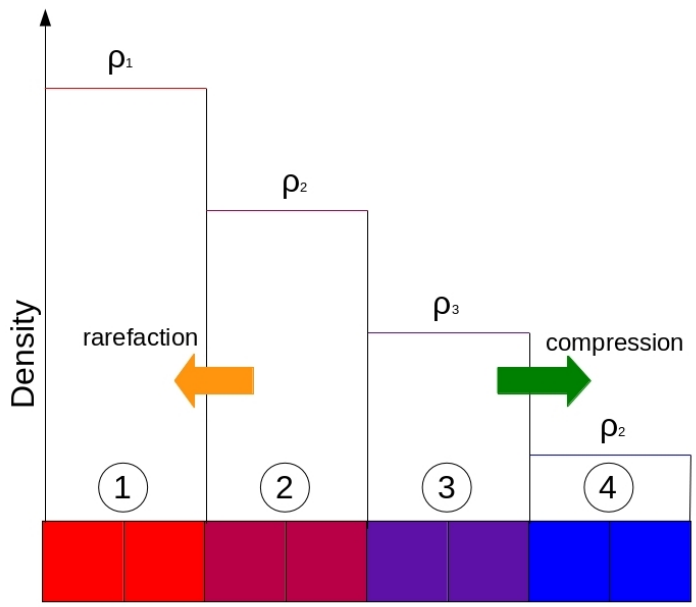

Figure 5.2. Regions within the shock tube based on rarefaction and compression

$$\frac{T_2}{T_1} = \frac{P_2}{P_1}\left(\frac{\frac{\gamma+1}{\gamma-1} + \frac{P_2}{P_1}}{1 + (\frac{\gamma+1}{\gamma-1})\frac{P_2}{P_1}}\right) \tag{5.5}$$

$$\frac{\rho_2}{\rho_1} = \frac{1 + (\frac{\gamma+1}{\gamma-1})\frac{P_2}{P_1}}{\frac{\gamma+1}{\gamma-1} + \frac{P_2}{P_1}} \tag{5.6}$$

$$W = a_1\sqrt{\frac{\gamma+1}{2\gamma}\left(\frac{P_2}{P_1} - 1\right) + 1} \tag{5.7}$$

$$P_2 = P_3 \tag{5.8}$$

$$\frac{P_3}{P_4} = \left(\frac{\rho_3}{\rho_4}\right)^{\gamma} = \left(\frac{T_3}{T_4}\right)^{\frac{\gamma}{\gamma-1}} \tag{5.9}$$

5.3 Results and Error

Enthlapy and density have a discontinuity as seen in figure 5.3 where the diaphragm was initially placed . Similarly there are discontinuities that move with the rarefacation and compression waves for pressure, density, and velocity. The largest error occurs around these discontinuities as seen in figure 5.4. A fine spatial mesh and a small time step are needed to accurately reflect the exact solution.

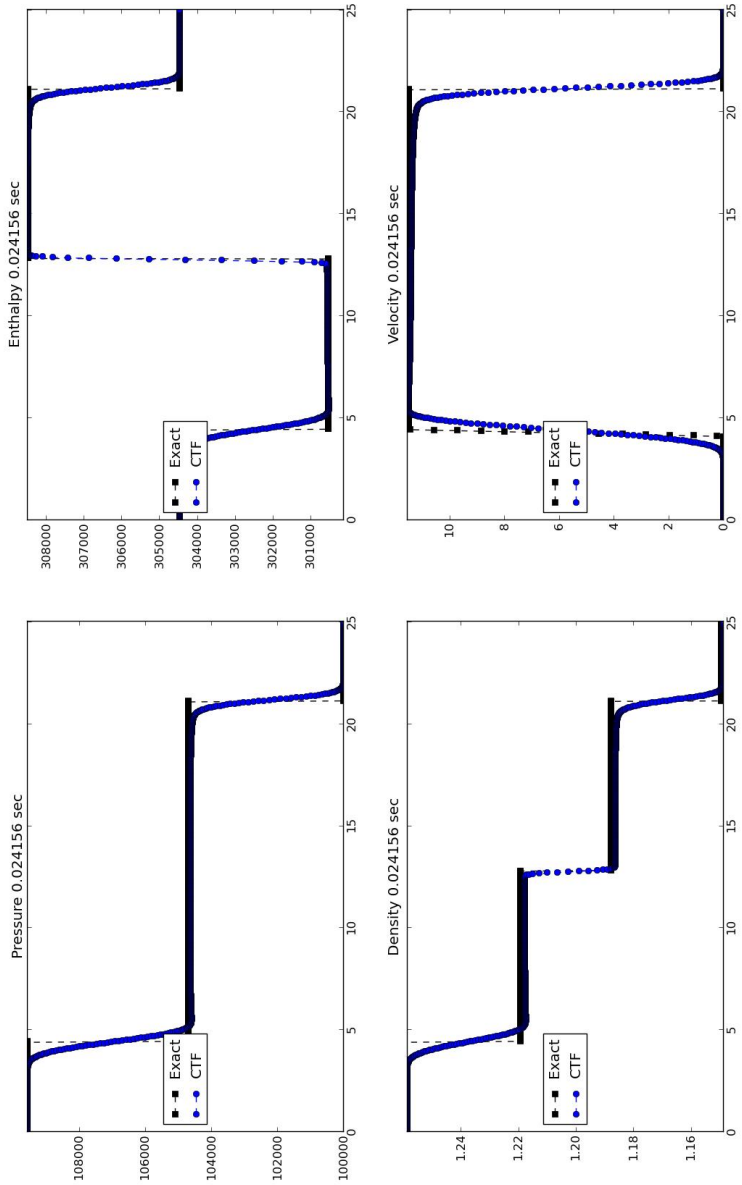

Figure 5.3. Comparison of analytical and numerical results for shock tube

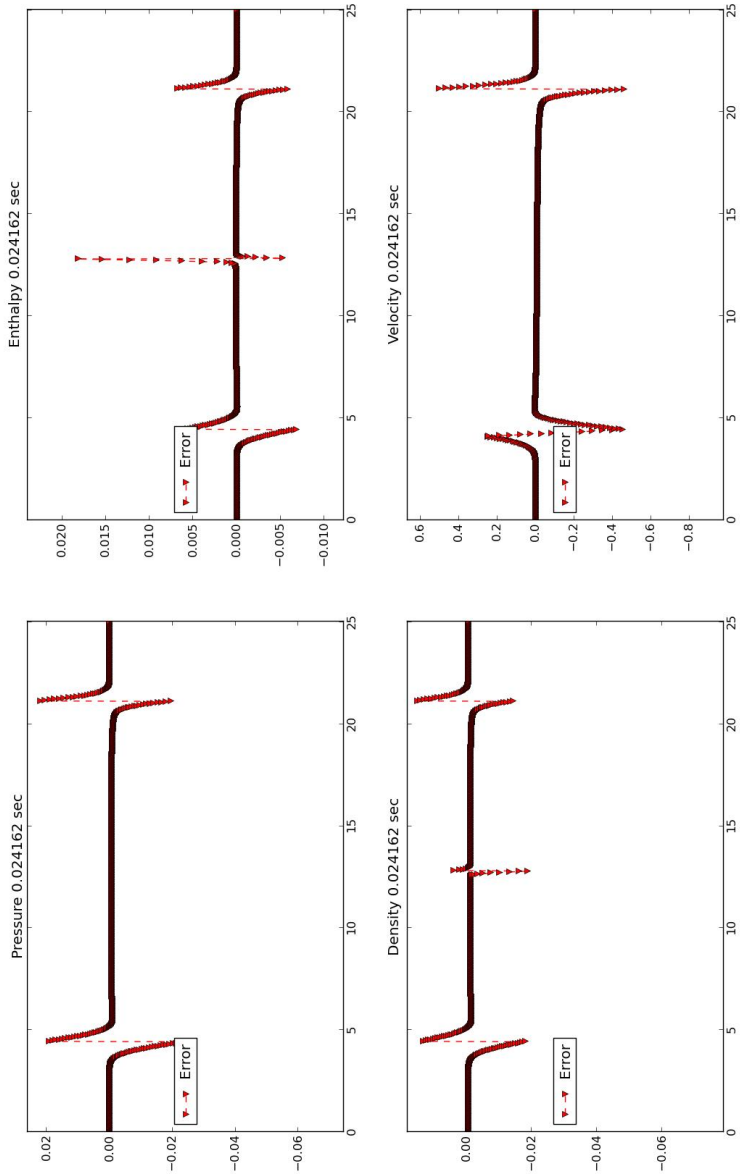

Figure 5.4. Truncation error for shock tube

5.4 Scaling of Error

A Richardson Extrapolation was performed on the density, enthalpy, and mass flow rate for the shock tube analysis in time. The error approaches zero as the time step size gets smaller as seen in figure 5.5. The order of accuracy with respect to time is converges to first order accurate as the time step size decreases. The range of time step values shown are within the asymptotic limit.

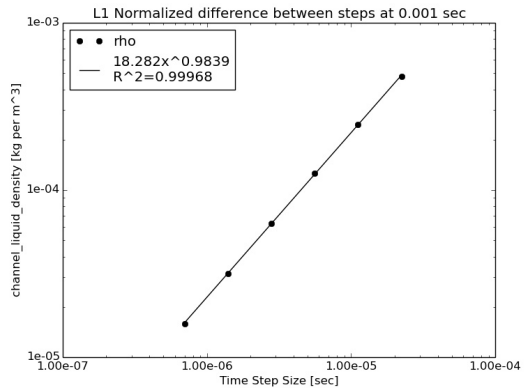

Figure 5.5. Richardson Extrapolation of the shock tube results N=50

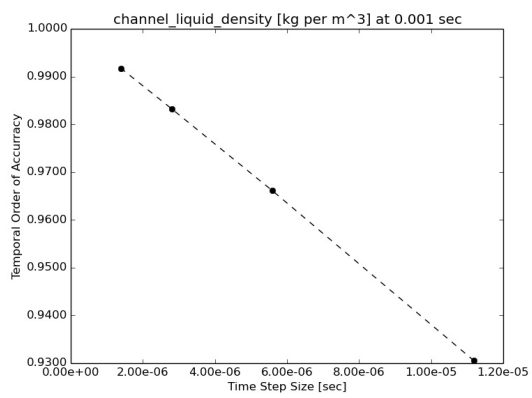

Figure 5.6. Temporal Order of Accuracy for shock tube

Chapter 6
Isokinetic Sine Wave Advection

The procedures that can be used for code verification, from least to most rigorous, include: expert judgment, error quantification, consistency/convergence, and order of accuracy [9]. For this work, the Richardson extrapolation will be used to check for convergence and order of accuracy of the error in space and time. The error should converge to zero, and the order of accuracy should converge to the values obtained through the modified equation analysis [10] at the end of this section.

6.1 Problem Setup

To obtain an analytical solution for a subchannel code, typically the method of manufactured solutions [11] is needed. To readily obtain an analytical solution and isolate only the mass and energy conservation equations, several simplifications to the verification problem are made. Only one channel is considered to make the problem 1-D. In order to make the problem perfectly isobaric and isokinetic, grid spacer losses, frictional losses, and gravity head losses are set to zero representing a smooth horizontal pipe. Small fluctuations in pressure and velocity may still occur due to the assumption that the EOS is linear. The channel geometry and operating conditions approximate a standard PWR as shown in table 6.1. The inlet of the channel has a constant velocity with a fluctuating enthalpy that corresponds to be near the standard PWR rod bundle coolant channel inlet conditions. The problem will aslo have constant axial spacing and time step size. The length of the transient was defined to be quadruple the time needed for the liquid at the inlet to advect to the outlet. The frequency of the sine wave was defined to generate a full period of a spatial wave across the length of the channel. With these simplifications, the method of manufacturing solutions is unnecessary since the known solutions are simply the advection of the transinet inlet conditions. The functions for the etnhalpy h and mass flow rate, $\dot{m}$, are given in equations 6.1 and 6.2 where x is the length from the inlet and t is the simulated time. The functions smoothly transition to the initial condition of a straight line across the domain. The enthalpy and mass flow rate vary proportionally to the density such that an isokinetic boundary condition is created at the inlet. While these simplifications do not model a realistic problem, they appropriately isolate the 1-D single phase mass and energy conservation equations for the

purpose of verification.

Table 6.1. Problem Parameters

Parameter	Symbol	Value	Unit
Axial Length	L	3.6586	m
Channel Area	A_{ch}	4.94E-005	m^2
Wetted Perimeter	P_w	1.49E-002	m
Velocity	V_o	7.35	$\frac{m}{s}$
Pressure	P_o	155.00	bar
Temperature 1	T_1	289.500	°C
Temperature 2	T_2	327.00	°C
Enthalpy 1	h_1	1281.55	$\frac{kJ}{kg}$
Enthalpy 2	h_2	1497.21	$\frac{kJ}{kg}$
Mass Flow Rate 1	$\dot{m}_1$	0.2713	$\frac{kg}{s}$
Mass Flow Rate 2	$\dot{m}_2$	0.2399	$\frac{kg}{s}$
Final Time	t_f	2.00	sec
Wave Frequency	ω	1.00	Hz

$$h(i,j) = \frac{1}{2}\left((h_1 + h_2) + (h_1 - h_2)cos\left(\omega\left(j\Delta t + \frac{i\Delta x}{V_o}\right)\right)\right) \tag{6.1}$$

$$\dot{m}(i,j) = \frac{1}{2}\left((\dot{m}_1 + \dot{m}_2) + (\dot{m}_1 - \dot{m}_2)cos\left(\omega\left(j\Delta t + \frac{i\Delta x}{V_o}\right)\right)\right) \tag{6.2}$$

The comparison between the data table and the output in CTF are shown for enthalpy and mass flow rate in figures 6.1 and 6.2, respectively. The CTF output was read from the high precision VTK data files at each point in time, which omitted the actual ghost cell where these values were applied. The CTF values are located at the nearest node to the inlet, and will experience small amounts of numerical diffusion. For large mesh sizes, this discrepancy is negligible as can be seen by the overlapping profiles in figures 6.1 and 6.2.

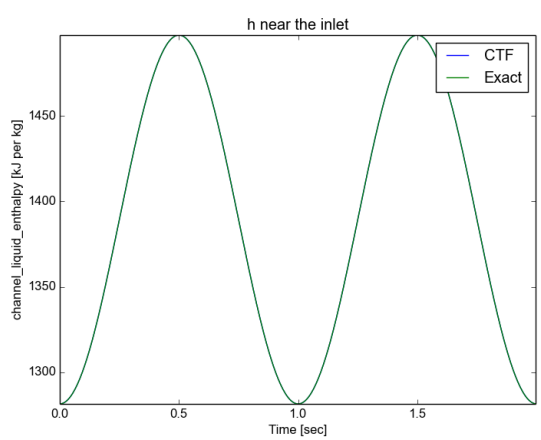

Figure 6.1. Enthalpy Near the Inlet and the Analytical Solution

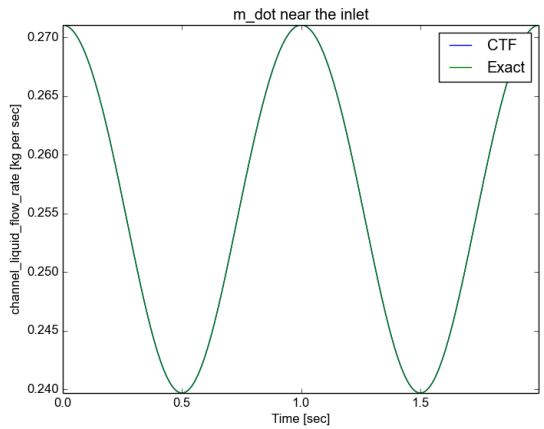

Figure 6.2. Density Near the Inlet and the Analytical Solution

The pressure and the velocity fluctuate by less than 0.25% during the simulation due to approximating the EOS as a linear function. This is considered small for this problem and should not greatly affect the order of accuracy of the error. The VTK output files allow for a high level of precision, reducing round off error in the output during the post processing.

6.2 Code Convergence

The current version of CTF uses global code convergence criteria that are used to estimate the rate of change of global mass and energy conservation. The transient values of these criteria are shown in figure 6.3 for the original version of CTF simulating the verification problem. Mass balance and storage are in units of $\frac{kg}{s}$. The energy balance, fluid energy, and solid energy are in units of kW. The solid energy storage is zero since there are not any heat structures present. The fluctuating values represent differences between the energy and mass entering and leaving the system. The flat profile for the mass storage term means that the sine wave has fully developed spatially through the channel.

The residual formulation prints out the summation of the equation residuals across the domain to an output file at the end of each time step and can be seen in figure 6.4. The mass equation residual is in units of $\frac{kg}{m^3 s}$. The energy equation residual is in units of $\frac{kW}{m^3}$. The momentum residual is in units of $\frac{kg}{m^2 s^2}$. The flat profile of the mass and energy residuals shows that the sine wave has fully developed spatially through the channel.

6.3 Modified Equation Analysis

The order of accuracy in time and space can be analytically determined for this problem through a modified equation analysis. Because the velocity is constant, it can be pulled out of the spatial derivative as shown in equation 6.3. Using upwinding, the finite difference can be written to look like equation 6.4. A second order Taylor series approximation can be used for ρ_i^{n+1} and ρ_{i-1}^n as

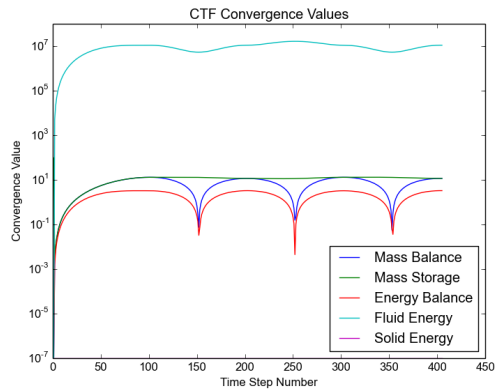

Figure 6.3. Code Convergence Criteria for the Original Version of CTF

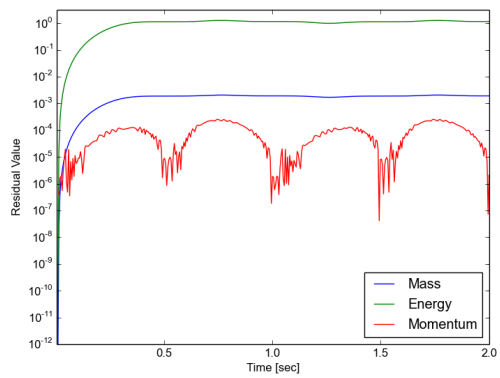

Figure 6.4. Summation of the Residuals for the Residual Version of CTF

shown in equations 6.5 and 6.6 respectively. The higher order terms ($O(\Delta x^2, \Delta t^2)$) are not taken into account for this approximation. The Taylor series approximations can then be substituted into 6.4 to yield 6.7. This is the beginning of the modified equation analysis. The goal will be to isolate the original PDE and define the truncation error.

$$\frac{\partial \rho}{\partial t} + U_0 \frac{\partial \rho}{\partial x} = 0 \tag{6.3}$$

$$\frac{\rho_i^{n+1} - \rho_i^n}{\Delta t} + U_0 \frac{\rho_i^n - \rho_{i-1}^n}{\Delta x} = 0 \tag{6.4}$$

$$\rho_i^{n+1} = \rho_i^n + \frac{\partial \rho}{\partial t}\Delta t + \frac{1}{2}\frac{\partial^2 \rho}{\partial t^2}\Delta t^2 + O(\Delta t^3) \tag{6.5}$$

$$\rho_{i-1}^n = \rho_i^n - \frac{\partial \rho}{\partial x}\Delta x + \frac{1}{2}\frac{\partial^2 \rho}{\partial x^2}\Delta x^2 + O(\Delta x^3) \tag{6.6}$$

The lengthy equation 6.7 can be reduced to equation 6.8 since the ρ_i^n terms subtract out and

the Δt and Δx terms in the denominator cancel out. This reduced equation can be re-written into equation 6.9, with the original PDE followed by the truncation terms.

$$\frac{\left(\rho_i^n + \frac{\partial \rho}{\partial t}\Delta t + \frac{1}{2}\frac{\partial^2 \rho}{\partial t^2}\Delta t^2\right) - \rho_i^n}{\Delta t} + U_0 \frac{\rho_i^n - \left(\rho_i^n - \frac{\partial \rho}{\partial x}\Delta x + \frac{1}{2}\frac{\partial^2 \rho}{\partial x^2}\Delta x^2\right)}{\Delta x} + O(\Delta x^2, \Delta t^2) = 0 \quad (6.7)$$

$$\frac{\partial \rho}{\partial t} + \frac{1}{2}\frac{\partial^2 \rho}{\partial t^2}\Delta t + U_0\left(\frac{\partial \rho}{\partial x} - \frac{1}{2}\frac{\partial^2 \rho}{\partial x^2}\Delta x\right) + O(\Delta x^2, \Delta t^2) = 0 \quad (6.8)$$

The terms to the right of the original PDE are the first order accurate truncation terms. Notice how the truncation error is dependent on both the on the second derivatives of density with respect to space and time, and on the numerical spacing Δt and Δx. Since the truncation error is linearly dependent on Δt and Δx, the order of accuracy is 1 with respect to time and space.

$$\frac{\partial \rho}{\partial t} + U_0\frac{\partial \rho}{\partial x} + \frac{1}{2}\frac{\partial^2 \rho}{\partial t^2}\Delta t - U_0\frac{1}{2}\frac{\partial^2 \rho}{\partial x^2}\Delta x + O(\Delta x^2, \Delta t^2) = 0 \quad (6.9)$$

When the energy equation undergoes a similar modified eqution analysis, the order of accuracy is also 1 for time and space. The momentum conservation equation does not apply for this problem since the velocity is constant.

6.4 Richardson Extrapolation

The Richardson extrapolation was performed by refining the spatial and temporal step sizes by a factor of 2 for a set number of times. The spatial and temporal studies are refined separately in their own study in order to isolate the spatial and temporal affects on the solution. The generation of the inputs, running of the codes, and analysis of the output were automated with a python script in order to reduce user input errors and increase repeatability. For this analysis, a significant amount of information was added to the hdf5 output files, increasing memory usage and run time. The computational resources for the spatial study was much higher than the temporal study due to the need to keep the courant number below 0.500. To keep the computational resources needed to perform this analysis reasonable, fewer spatial refinements were performed compared to the temporal analysis.

6.5 Convergence of Error

The difference between iterations was computed at each time step and spatial location for each quanitity of interest. This difference is considered as the error between each iteration. For the spatial refinement, the lower iterate values were numerically integrated to match the shape of the initial domain. The errors were then summed over the entire domain to yield a total error for each variable. The total error for density is plotted in figures 6.5 and 6.6 as a function of

temporal and spatial step size.

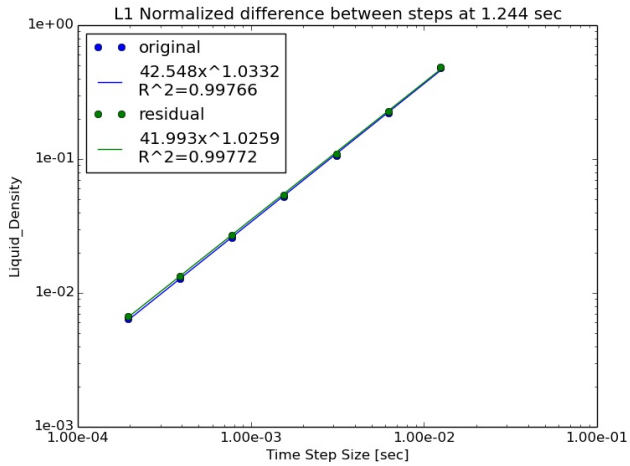

Figure 6.5. Difference Between Successive Temporal Refinements for Density

The data points were chosen to be inside of the asymptotic range as shown by the good power fit with an exponent near 1. The power fit shows that as the temporal and spatial step sizes are reduced, the numerical error approaches zero. The discretization error between the original version of CTF is relatively small and is most likely due to the small fluctuations in the velocity present in the original version of the code.

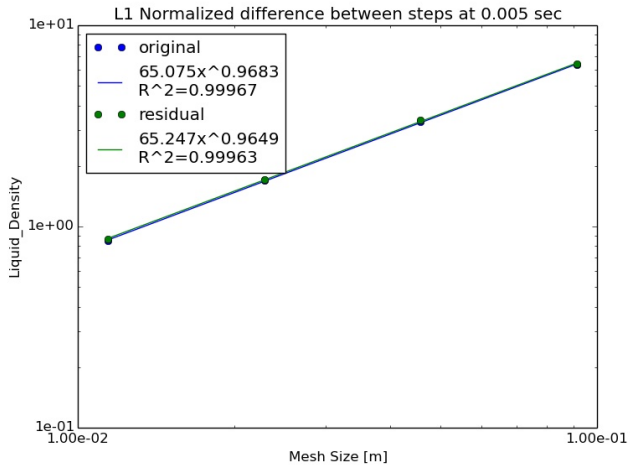

Figure 6.6. Difference Between Successive Spatial Refinements for Density

6.6 Order of Accuracy

The order of accuracy for this verification problem is first order as shown by the modified equation analysis. This can be considered to be the exponent on the power fits as seen in figures 6.5. However the order of accuracy p can be calculated by using equation 6.10 where f_1, f_2, f_3 are consecutive levels within the same Richardson extrapolation study. The refinement factor, R, has the constant value of 2 for both the spatial and temporal studies.

$$p = \frac{ln\left(\frac{f_3 - f_2}{f_2 - f_1}\right)}{ln(R)} \tag{6.10}$$

The order of accuracy for all of the variables are presented for the temporal analysis and spatial analysis in figures 6.7 and 6.8 respectively. The temporal order of accuracy is well within the asymptotic range for the whole analysis, and moves closer to 1.0 with decreasing time step size. The spatial order of accuracy is a slightly outside the asymptotic range, but approaches an order of accuracy of 1.0 with decreasing mesh size.

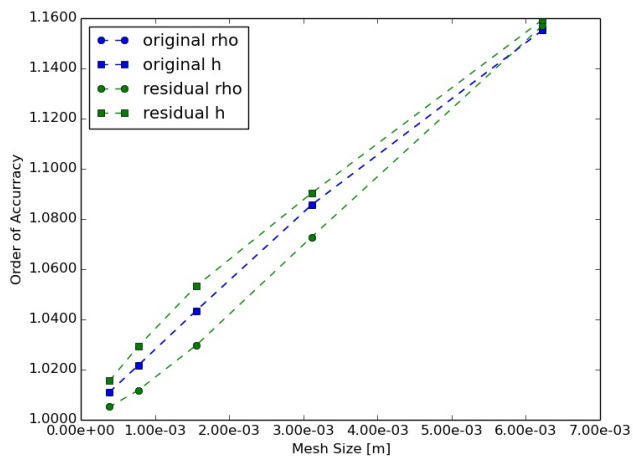

Figure 6.7. Temporal Order of Accuracy

The slight differences between the original version of CTF and the residual formulation might be due to the different solution methods and back substitution of variables. Despite the small differences, both versions of the code exhibit order of accuracies very close the values obtained through the modified equation analysis.

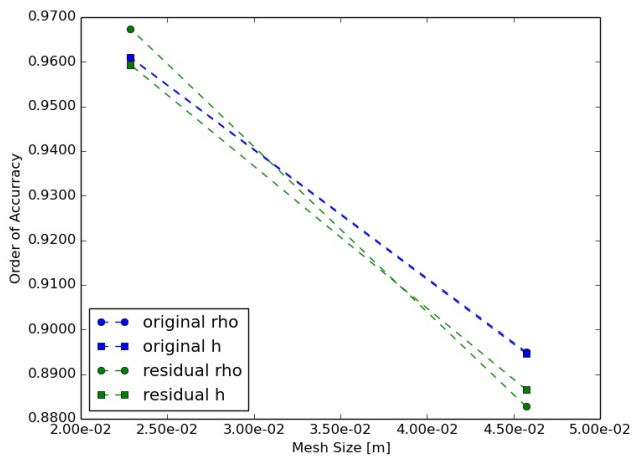

Figure 6.8. Spatial Order of Accuracy

Chapter 7
Uniform Heating Problem

7.1 Problem Setup

The test problem is a nuclear rod with uniform heat generation with parameters given in Table 7.1. The fuel and cladding are assumed to have constant material properties. The mass flow rate, reference pressure, and inlet temperature approximate normal PWR operating conditions. However, the heat generation rate is much less than normal PWR operating conditions to ensure that the problem remains well within the single-phase regime with an expected outlet temperature of under 300.0 $°C$. Additionally, the problem is set up so that the calculation of the heat transfer coefficient using the Dittus-Boelter correlation is appropriate. The subchannel is rod centered with no grid spacers or frictional losses. Gravity pressure losses in the vertical direction are taken into account.

Table 7.1. Problem Parameters

Parameter	Symbol	Value	Unit
Mass Flow Rate	$\dot{m}$	0.300	$\frac{kg}{sec}$
Pressure	P_o	165.00	bar
Inlet Temperature	T_{inlet}	290.00	°C
Linear Heat Rate	q'	4.00	$\frac{kW}{m-rod}$
Active Fuel Length	L	3.658	m
Fuel Radius	r_{fuel}	0.4096	cm
Outer Cladding Radius	r_{co}	0.475	cm
Inner Cladding Radius	r_{ci}	0.4174	cm
Rod Pitch	p	12.60	cm
Clad Specific Heat	$c_{p,clad}$	0.431	$\frac{kJ}{kg-K}$
Clad Density	ρ_{clad}	8470.57	$\frac{kg}{m^3}$
Clad Thermal Conductivity	k_{clad}	14.83	$\frac{W}{m-k}$
Fuel Specific Heat Capacity	$c_{p,fuel}$	0.289	$kJ/kg-K$
Fuel Density	ρ_fuel	10970.40	$\frac{kg}{m^3}$
Fuel Thermal Conductivity	k_fuel	14.83	$\frac{W}{m-k}$
Gap Heat Transfer Coefficient	h_{gap}	5678.30	$\frac{W}{m^2-K}$

7.2 Steady State Analytical Solution

At steady state conditions and for uniform heat generation, the original conduction equation can be integrated to obtain equation 7.1 for $0.0 \leq r < r_{fuel}$.

$$T_{rod}(r,z) - T_{rod}(r_{fuel},z) = \frac{q''' r_{fuel}^2}{4k_{fuel}} \left(1 - \frac{r^2}{r_{fuel}^2}\right) \tag{7.1}$$

The temperature at the fuel surface can be calculated from the cladding inner surface temperature and the thermal resistance across the gap as given in equation 7.2 for $r_{fuel} \leq r < r_{ci}$.

$$T_{rod}(r_{fuel},z) - T_{rod}(r_{ci},z) = \frac{q'}{2\pi r h_{gap}} \tag{7.2}$$

The temperature at the inner surface of the cladding can be calculated from the cladding inner surface temperature and the thermal resistance across the cladding as given by equation 7.3 for $r_{ci} \leq r < r_{co}$.

$$T_{rod}(r_{ci},z) - T_{rod}(r_{co},z) = \frac{q'}{2\pi k_{clad}} \tag{7.3}$$

The temperature at the outer surface of the cladding can be calculated from the fluid temperature and the thermal resistance due to convection as given by equation 7.4 for $r = r_{co}$.

$$T_{rod}(r_{co},z) - T_{fluid}(z) = \frac{q'}{2\pi r_{co} h_{fluid}} \tag{7.4}$$

The temperatures can be computed by working from the known fluid temperature, and working solving for temperatures from the outside surface of the cladding to the center of the fuel.Notice that the difference between any radial temperature and the fluid temperature at the same axial level is independent of the axial height. This difference will be compared first to verify that the conduction equation is working properly

7.3 Steady State Results

The temperature distribution within the fuel rod relative to the wall surface temperature can be seen in Figure 7.1. The analytical solution matches well with the different solution methods both within the fuel and at the cladding surfaces. The difference between the analytical solution and the numerical solutions are highest at the fuel centerline as can be seen by figure 7.2. This error is due to the numerical error from the finite differencing approximations made within the fuel. The fuel centerline temperature is extrapolated from the first and second nodal temperatures using a second order accurate forward differencing approximation of the boundary condition in equation 2.14. Normally CTF uses a different extrapolation method, but to consistently compare to the residual formulation was not used.

The relative error given in Table 7.2 is shown to scale with the inverse of the number of radial nodes in the fuel. The relative error does not scale with heat flux, but the temperature gradient

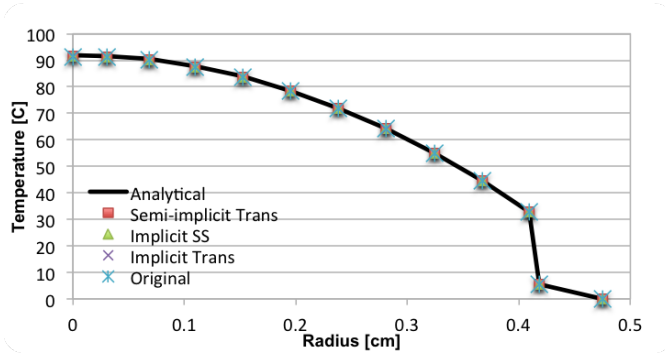

Figure 7.1. Steady State Radial Temperature Distribution Difference to Rod Surface Temperature

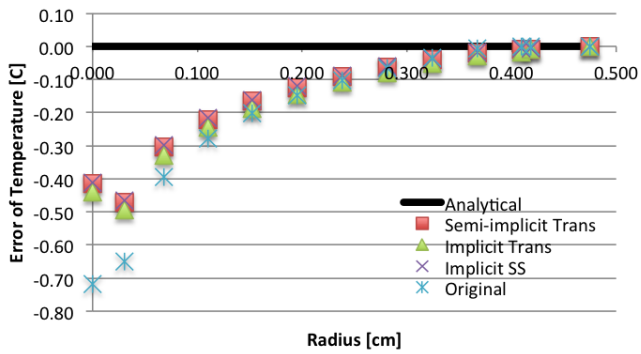

Figure 7.2. Error of Different Numerical Methods to Analytical Solution

from the fuel centerline to the rod wall does. The numerical error will also change for non-uniform heating and variable material properties within the fuel. The implicit transient solution method has slightly higher numerical error than the semi-implicit transient and implicit steady state solution methods. However, all three residual formulation methods have lower numerical error compared to the original steady state method from CTF. The order of accuracy is difficult to compute, since CTF uses non-uniform meshing near the rod center and since the fuel centerline temperature is extrapolated using a second order accurate method. The non-uniform mesh size also means that a Richardson extrapolation is not valid.

Table 7.2. Relative Error of Difference Between Fuel Centerline to Rod Surface Temperature

NR	SI Trans	I Trans	I SS	Original SS
5	1.33 %	1.35%	1.32%	2.15%
10	0.45 %	0.48%	0.45%	0.78%
20	0.15 %	0.18%	0.14%	0.20%

While there is on solid conduction in the axial direction, the fluid will have a temperature gradient in the axial direction. This will cause a 2-D temperature distribution as shown by Figure 7.3. The fluid temperature only changes by about 10 $°C$ from the inlet to the outlet, but the fuel temperature changes by about 90 $°C$ from the outer surface of the cladding to the fuel centerline

temperature. The hottest location of the fuel is located on the centerline at the top of the rod. The centerline fuel temperature is slightly under predicted by both the residual formulation and the original versions of CTF. However as table 7.2 shows, this is attributable to numerical error.

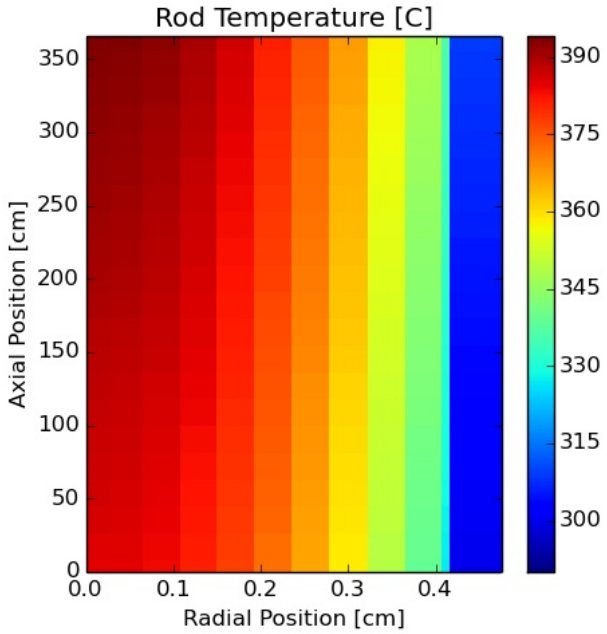

Figure 7.3. Steady State Axial and Radial Temperature Distribution in the Fuel Rod

7.4 Transient Results

The transient simulations were run for 30.0 seconds to reach a pseudo-steady state condition. The rate of change of the temperatures have reached near steady state conditions as shown by Figure 7 were the red lines are fuel node temperatures, and the black lines are cladding node temperatures. The semi-implicit method is used on the left, and the fully implicit method is on the right. For the semi-implicit solution method, a maximum time step size of 0.02 sec was needed to ensure stability. For the implicit solution method time step sizes well over 0.2 seconds could be taken. For the data in the figure, time steps of 1.0 second were used. The implicit Jacobian matrix is stiffer than the Jacobian matrix for the semi-implicit method and therefore takes longer to solve. Additionally, for time steps with large residuals multiple up to 5 iterations are needed. However the advantage of being able to take significantly longer time steps makes up for the increased computational cost per time step required by the semi-implicit method. The temperatures gained from the semi-implicit method and the implicit methods do not differ by significant amounts.

The transient behavior of temperature profile is shown in Figure 8 where the flat green line is the initial condition, the red line is the final profile, and the black lines are intermediate time steps. It is easier to observe the difference in the number of time steps between the semi-implicit

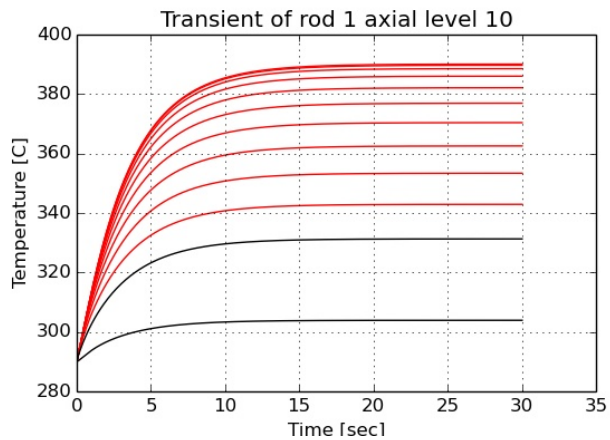

Figure 7.4. Plot of the Radial Nodal Temperatures for the Semi-Implicit Method

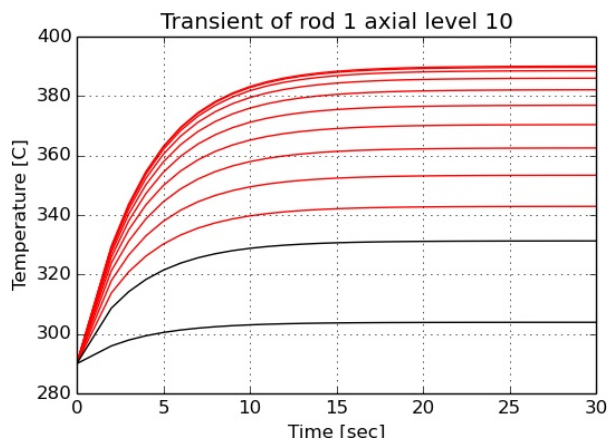

Figure 7.5. Plot of the Radial Nodal Temperatures for the Implicit Method

method on the left and the implicit method on the right. The intermediary time steps are still the same, as is the final solution. However, the implicit method will have greater numerical error compared to the semi-implicit method.

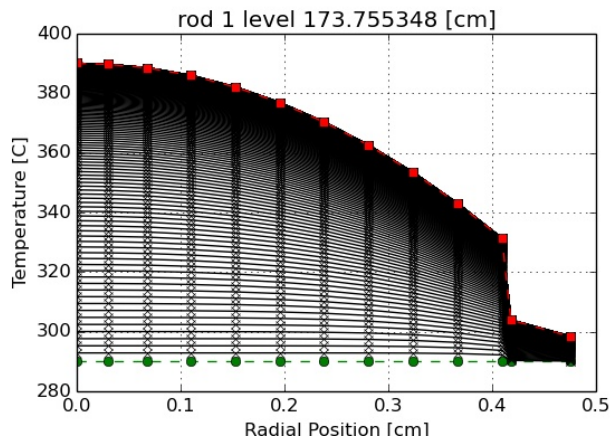

Figure 7.6. Temperature profile over time for the Semi-Implicit Method

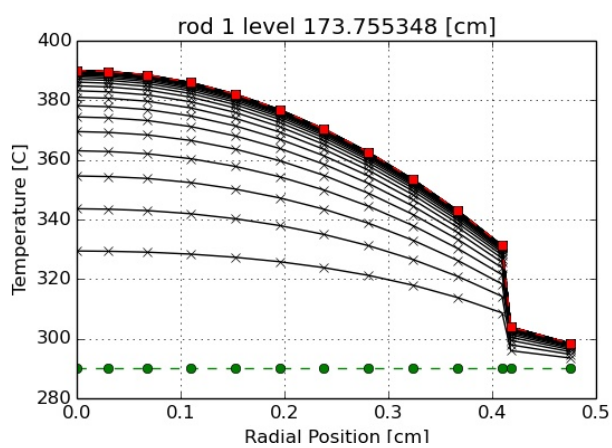

Figure 7.7. Temperature profile over time for the Implicit Method

Bibliography

[1] Salko, R. K. (2014) "CTF Theory Manual," (814).

[2] Lloyd, L. J. (2014) "Development of a Spatially-Selective, Nonlinear Refinement Algorithm for Thermal-Hydraulic Safety Analysis," .

[3] Aumiller, D. L., G. W. Swartele, F. X. Lane, J. W. Buschman, and M. Meholic (2013) "Development of Verification Testing Capabilities for Safety Codes," *NURETH-15*.

[4] Roy, C. J. (2005) "Review of code and solution verification procedures for computational simulation," *Journal of Computational Physics*, **205**, pp. 131–156.

[5] Merroun, O., A. Almers, T. E. Bardouni, B. E. Bakkari, and E. Chakir (2009) "Analytical benchmarks for verification of thermal-hydraulic codes based on sub-channel approach," *Nuclear Engineering and Design*, **239**, pp. 735–748.

[6] Mahadevan, V., V. Mousseau, and J. C. Ragusa (2009) "Verification of multiphysics software: Space and time convergence studies for nonlinearly coupled applications," *International Conference on Mathematics, Computational Methods & Reactor Physics*.
URL `http://mathematicsandcomputation.cowhosting.net/MC09/pdfs/201961.pdf`

[7] Botte, G., J. Ritter, and R. White (2000) "Comparison of finite difference and control volume methods for solving differential equations," *Computers and Chemical Engineering*, **24**, pp. 2633–2654.

[8] Anderson, J. D. (1990) *Modern Compressible Flow With Historical Perspective*, McGraw-Hill Inc.

[9] Oberkampf, W. L. and T. G. Trucano (2008) "Verification and Validation Benchmarks," *Nuclear Engineering and Design*, **238**, pp. 716–743.

[10] Villatoro, F. and J. Ramos (1999), "On the method of modified equations. I: Asymptotic analysis of the Euler forward difference method," .

[11] Salari, K. and P. Knupp (2000) *Code Verification by the Method of Manufactured Solutions*, *Tech. Rep. SAND2000-1444*, Aerosciences and Compressible Fluid Mechanics Department, Parallel Computing Sciences Department at Sandia National Laboratories, P.O. Box 5800, Albuquerque, NM 87185-0825.